NJC

ROYAL SOCIETY OF CHEMISTRY

PAPER

View Article Online
View Journal | View Issue

Cite this: *New J. Chem.*, 2025, **49**, 12140

Multistate luminescent probe: ICT-driven dual ESIPT-AIE for selective fluoride and cyanide ion recognition†

Aastha Palta,‡[a] Gulshan Kumar,[b] Kamaldeep Paul[a] and Vijay Luxami*[a]

Received 2nd January 2025,
Accepted 9th June 2025

DOI: 10.1039/d5nj00019j

rsc.li/njc

A highly selective and sensitive fluorescent chemosensor, **HNBZT**, has been designed and developed for the detection of F^- and CN^- ions. **HNBZT** exhibits excited-state intramolecular proton transfer (ESIPT), intramolecular charge transfer (ICT), and aggregation-induced emission (AIE) phenomena on a single molecular platform. Its photophysical and sensing behaviour has been evaluated using absorption and fluorescence spectroscopy. Notably, **HNBZT** displays a ratiometric fluorescence "turn-on" response to both anions in a CH_3CN solvent system. The binding of F^- and CN^- ions to **HNBZT** results in distinct absorption and emission colour changes, attributed to the unique electronic and structural perturbations induced by their respective interactions, facilitating visual detection. The lowest detection limits for F^- and CN^- ions are 7.6×10^{-8} M and 1.1×10^{-7} M, respectively. The coherence between the DLS and FESEM results underscores the consistency and reliability of the observed aggregation behaviour of **HNBZT**. ^{1}H NMR titrations of **HNBZT** with F^- and CN^- ions reveal distinct binding mechanisms, with F^- ions forming hydrogen bonds, while CN^- ions induce nucleophilic addition, which is also supported by theoretical studies. The binding stoichiometry of **HNBZT** with F^- and CN^- ions is determined to be 1 : 1 using Job's plot analysis.

1. Introduction

In the field of molecular design, there is a growing interest in developing compounds with multiple functionalities, capable of exhibiting diverse photophysical phenomena simultaneously. Among these phenomena, excited-state intramolecular proton transfer (ESIPT), intramolecular charge transfer (ICT), and aggregation-induced emission (AIE) stand out as key areas of exploration, offering flexible platforms for various applications ranging from sensing to optoelectronic devices.[1–6] Integrating these phenomena within a single molecular framework not only enhances their individual capabilities, but also reveals emergent properties to opening up new possibilities for advanced molecular sensing.

ESIPT, ICT, and AIE are three key phenomena shaping the development of fluorescent probes and materials.[7–10] ESIPT facilitates the transfer of a proton between two molecular sites upon photoexcitation, inducing significant structural and electronic changes in excited states, thereby altering their photophysical properties like emission wavelength and intensity.[11–15] Similarly, ICT involves the redistribution of electron density upon photoexcitation, offering a versatile platform for controlling charge transfer processes within molecules and enabling substantial changes in absorption and emission spectra.[16–19] Furthermore, the AIE phenomenon enhances light emission intensity upon aggregation, diverging from conventional fluorophores that often undergo fluorescence quenching in aggregated states. This transformative property of AIE-active molecules makes them highly attractive for diverse applications including biological imaging, chemical sensing, and optoelectronic devices.[20–25]

The emergence of molecules with double ESIPT, ICT, and AIE properties presents an exciting opportunity to combine these phenomena and unlock novel functionalities. Such molecules hold great promise for applications requiring multifunctionality, including simultaneous detection of ions.[26,27] Detecting different ions is crucial for environmental monitoring, biomedical diagnostics, and industrial safety due to their significance as indicators of water quality, environmental contamination, and chemical toxicity.[28–30]

The selective detection of anions, such as fluoride (F^-) and cyanide (CN^-), is of significant interest due to their unique chemical properties and widespread relevance in environmental, biological, and industrial processes.[31–33] For example,

---

[a] *Department of Chemistry and Biochemistry, Thapar Institute of Engineering and Technology, Patiala, 147004, India. E-mail: vluxami@thapar.edu*
[b] *Department of Chemistry, Banasthali University, Banasthali Newai, 304022, Rajasthan, India*

† Electronic supplementary information (ESI) available. See DOI: https://doi.org/10.1039/d5nj00019j

‡ Current address: University Centre for Research and Development, Chandigarh University, Mohali, 140413, India.

fluoride ions play a critical role in dental care, such as water fluoridation, and are used in various industrial applications, while cyanide is known for its toxicity, yet it is widely utilized in gold mining and chemical synthesis.[34–36] As a result, the development of sensitive and selective methods for detecting these anions is essential for both environmental monitoring and safety.[37,38]

The challenge lies in designing a sensor that can selectively interact with both anions despite their distinct sizes, geometries, and chemical behaviors. Fluoride is a small, highly electronegative ion, whereas cyanide is larger, less electronegative, and can engage in both hydrogen bonding and covalent interactions. A well-designed chemosensor must not only recognize these differences but also exhibit distinct, measurable responses to each anion.

This study introduces a novel fluorescent chemosensor capable of differential sensing for F^- and CN^- ions with exceptional selectivity and sensitivity. **HNBZT** showed ESIPT, ICT, and AIE phenomena within a single molecular framework. Furthermore, **HNBZT** exhibited a ratiometric fluorescence "turn-on" response to both anions when dissolved in CH_3CN solvent. Moreover, we elucidated **HNBZT**'s stoichiometry in interaction with F^- and CN^- ions through Job's plot analysis. This comprehensive investigation illuminates the multifaceted behavior of **HNBZT**.

2. Experimental section

2.1. Materials and instruments

All chemicals and solvents used in the experimental work were of analytical grade and were procured from Sigma-Aldrich, Spectrochem, and Rankem Ltd, depending on availability. These were used without further purification. The progress of the chemical reactions was monitored using thin layer chromatography (TLC). Melting points were recorded using the open capillary method and were uncorrected. The synthesized compounds were characterized using NMR spectroscopy on a JEOL ECS-400 MHz instrument in DMSO-d_6 with TMS as the internal standard. HRMS spectra were obtained using an XEVO G2-XS QTOF of WATERS. Absorption studies were performed with a SHIMADZU UV-2600 spectrophotometer, employing quartz cells with a 1 cm path length. Fluorescence studies were conducted using an Agilent Technologies Cary Eclipse Spectrophotometer, with excitation and emission slit widths set to 5 nm each. Absorption and emission scans were saved as ACS files and subsequently processed in Excel™ to generate the presented graphs. The stoichiometry of the complexes was analyzed using Job's plot analysis. Time-resolved fluorescence studies were carried out using a DeltaFlex Modular Fluorescence Lifetime Spectrofluorimeter from HORIBA Scientific. The FE-SEM analysis was carried out using a ZEISS MERLIN Compact field emission-scanning electron microscope.

2.2. Solutions for absorption and emission studies

The stock solution of **HNBZT** was prepared in $CH_3CN:DMSO$ (9.5 : 0.5) at 10^{-3} M concentration. Tetrabutyl ammonium salts of F^-, Cl^-, CN^-, Br^-, I^-, SCN^-, AcO^-, NO_3^-, $P_2O_7^{4-}$, $H_2PO_4^-$, and HSO_4^- were used for anions. The stock solutions of the anions were prepared in acetonitrile at 10^{-1} M concentration. As needed, the stock solutions were further diluted to the desired concentration.

2.3. Calculation of binding constants and detection limits

The binding constants were calculated using the Benesi–Hildebrand method using eqn (1) where I_0, I, and $I_{\max}$ are the absorption/emission intensities of the compound in the absence of analyte, at an intermediate, and at complete titration with the analyte, respectively. K_a is the binding constant; C is the concentration of analyte and n is the number of analytes bound per molecule.

$$\frac{1}{I - I_0} = \frac{1}{K_a(I_{\max} - I_0)[C]^n} + \frac{1}{I_{\max} - I_0} \tag{1}$$

Limit of detection (LOD) was determined from the following equation:

$$\mathrm{DL} = \frac{3 \times \text{standard deviation of the blank solution}}{\text{slope of calibration curve}} \tag{2}$$

2.4. Synthetic procedure for HNBZT

Compound **1a**[39] (200 mg, 0.8 mmol) and 2-hydroxy-1-naphthaldehyde (156 mg, 0.9 mmol) were stirred at 70 °C in ethanol for 3 h (Scheme 1). On completion, the reaction mixture was cooled at room temperature, and the crude solid was filtered and washed with ethanol to obtain an orange coloured solid of **HNBZT** in 85% yield. M.p. 270–275 °C; ^{1}H NMR (DMSO-d_6, 400 MHz): δ (ppm) 9.63 (d, 1H, J = 8.0 Hz, –CH=N), 8.48 (d, 1H, J = 8.0 Hz, ArH), 8.22 (d, 1H, J = 7.8 Hz, ArH), 8.13 (d, 1H, J = 8.0 Hz, ArH), 8.05 (d, 1H, J = 8.0 Hz, ArH), 7.92 (d, 1H, J = 12.0 Hz, ArH), 7.76 (dd, 1H, ^1J = 3.4 Hz, ^2J = 8.0 Hz, ArH), 7.54–7.50 (m, 2H, ArH), 7.44–7.42 (m, 1H, ArH), 7.34–7.30 (m, 2H, ArH), 7.24 (d, 1H, J = 4.0 Hz, ArH), 6.95 (d, 1H, J = 7.4 Hz, ArH) (Fig. S1, ESI†). ^{13}C NMR (DMSO-d_6, 100 MHz): δ (ppm) 173.1, 165.4, 157.9, 155.4, 151.9, 147.1, 138.4, 134.5, 133.7,

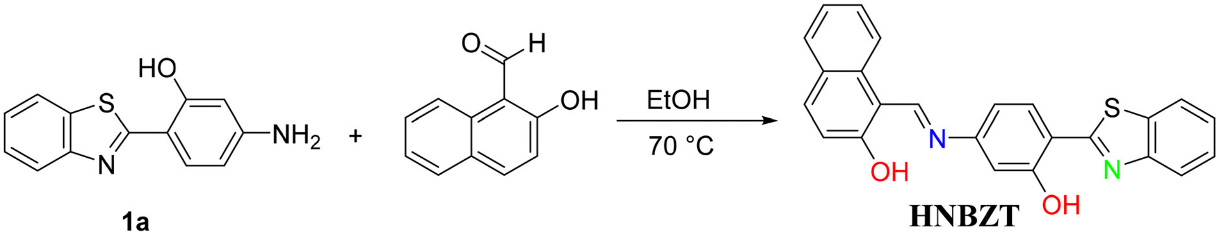

Scheme 1 Synthesis of **HNBZT**.

130.3, 129.6, 128.8, 127.1, 125.6, 124.3, 123.2, 122.5, 121.0, 116.9, 112.5, 109.1, 108.6 (Fig. S2, ESI†). HRMS (ESI-TOF): (*m*/*z*) $[M + H]^+$ calcd for $C_{24}H_{17}N_2O_2S$: 397.1007, found: 397.1015 (Fig. S3, ESI†). **FT-IR** (cm^{-1}): 3462 ($\nu_{O\text{–}H}$), 3204 ($\nu_{C\text{–}H\ str.}$, aromatic), 2969 ($\nu_{C\text{–}H\ str.}$, aromatic), 1573 ($\nu_{C=NH}$), 1343 ($\nu_{C\text{–}C}$), (Fig. S4, ESI†).

2.5. Real sample analysis

For the practical application of **HNBZT** for detecting F^- and CN^- ions, water samples were collected from different sources. The qualitative applications of F^- and CN^- ions were estimated through a calibration curve. All these samples were further spiked with different concentrations of F^- and CN^- ions (20 μM and 40 μM). **HNBZT** (20 μM) was added to these solutions (3 mL) having different F^- and CN^- ion concentrations. The spiked samples were estimated using the calibration curve.

3. Results and discussion

3.1. Photophysical properties of HNBZT

The photophysical properties of **HNBZT** were investigated using absorption and emission spectroscopy. The absorption spectrum of **HNBZT** (20 μM) in CH_3CN displayed a high-energy transition band at 400 nm and two low-energy transition bands at 445 nm and 475 nm. Upon excitation at 400 nm, **HNBZT** (20 μM) exhibited an emission band at 505 nm, corresponding to a Stokes shift of 105 nm. Due to the presence of electron donor and acceptor units, an intramolecular charge transfer (ICT) process is likely enabled in **HNBZT**. To explore the influence of ICT on steady-state absorption and emission spectra, various solvents with differing polarities were employed. In non-polar solvents, the absorption peak was observed at 400 nm. However, as solvent polarity increased, the absorption maximum red-shifted to 475 nm, accompanied by an enhancement of a shoulder band at 535 nm (Fig. 1a). This red shift in absorption maxima is attributed to the ICT process, involving electron transfer from the hydroxy naphthalene unit to the benzothiazole moiety. Similarly, while the emission maxima were predominantly at 505 nm in most solvents, they shifted to 535 nm in CH_3OH and 560 nm in H_2O as the solvent polarity increased (Fig. 1b, Table 1). These shifts in emission maxima further support the presence of ICT in the excited state. Additionally, **HNBZT** exhibited noticeable color changes from light yellow to orange with increasing solvent polarity (Fig. 1c), providing a visual indication of the ICT process.

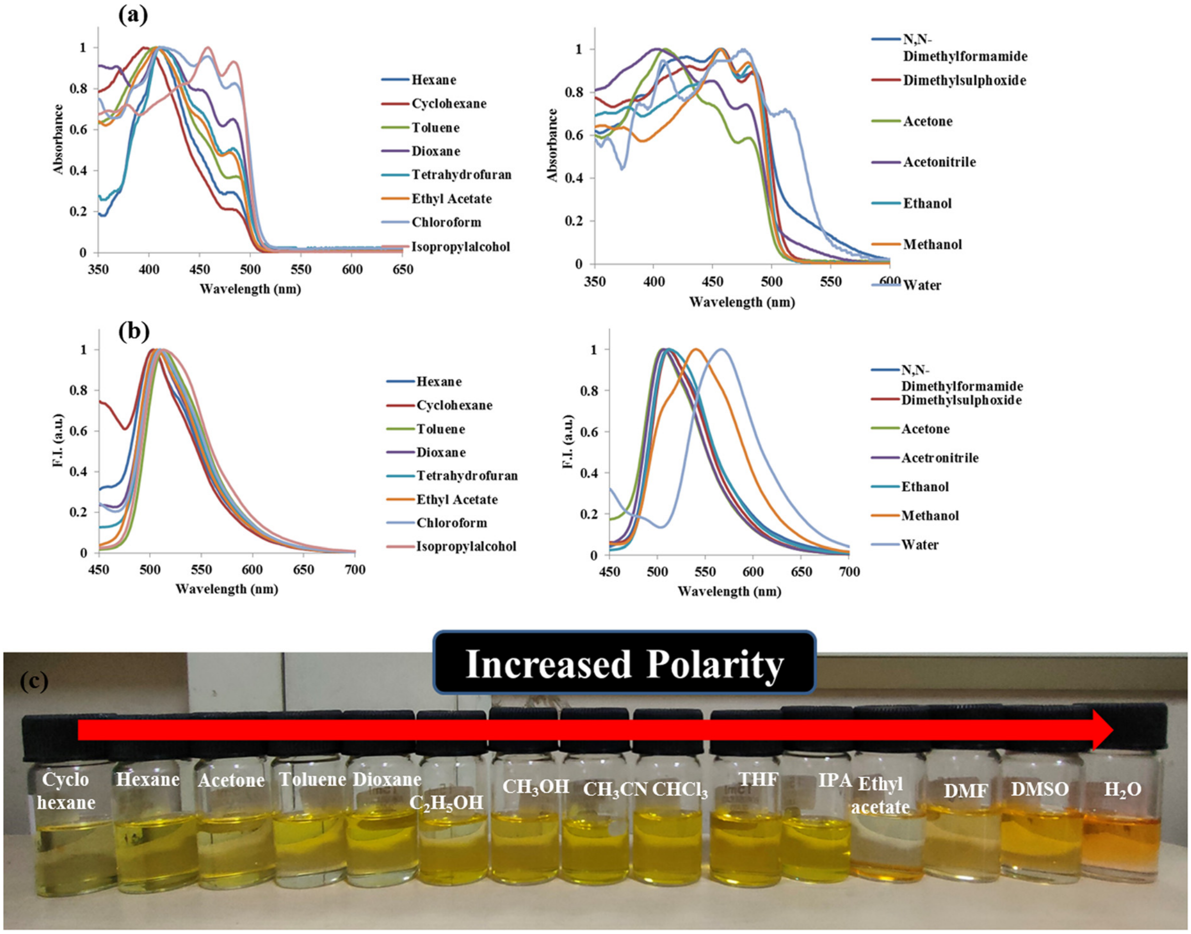

Fig. 1 (a) Absorption and (b) emission spectra of **HNBZT** (20 μM) in solvents of different polarity, and (c) colorimetric response of **HNBZT** (20 μM) upon increasing polarity of the solvents.

Table 1 Photophysical properties of **HNBZT**

S. no.	Solvent	λ_{max} (nm)	Molar absorptivity ε (M^{-1} cm^{-1})	λ_{em} (nm)	Stokes shift $\Delta\nu$ (cm^{-1})	Quantum yield (Φ)
1	Hexane	405	6050	505	4890	0.49
2	Cyclohexane	405	16 300	505	4890	0.45
3	Toluene	405	19 500	509	4890	0.51
4	Chloroform	405	14 900	509	4890	0.59
5	Tetrahydrofuran	405	5300	510	4890	0.53
6	Acetone	405	15 550	507	4890	0.55
7	Dioxane	405	15 700	508	4890	0.55
8	Ethyl acetate	405	19 550	511	4890	0.56
9	Dimethylsulphoxide	455	17 550	513	2180	0.48
10	*N*,*N*-Dimethylformamide	455	15 300	515	2180	0.54
11	Acetonitrile	405	16 900	506	4890	0.72
12	Isopropylalcohol	475	15 400	507	1250	0.75
13	Ethanol	455	18 350	515	2180	0.58
14	Methanol	475	16 100	535	2360	0.65
15	Water	475	5300	560	3190	0.69

Stokes shift = $1/(\lambda_{em} - \lambda_{max})$, reference for quantum yield is quinine sulphate.

HNBZT exhibited torsional flexibility concerning single bonds, specifically C—N rotation at the imine center connection and C—C rotation at the benzothiazole unit connection, which resulted in different conformations. The theoretical calculations indicate that the plausible configurations, which were optimized at the S_0 state, have a significant population of 55% and 45%, respectively, and are relatively stable due to the formation of strong intramolecular hydrogen bonding in the **HNBZT-I** and **HNBZT-II** conformers. In the S_0 state with no imaginary frequency, **HNBZT**'s geometry was slightly twisted in both of these configurations.

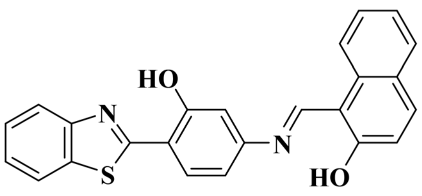

HNBZT-I

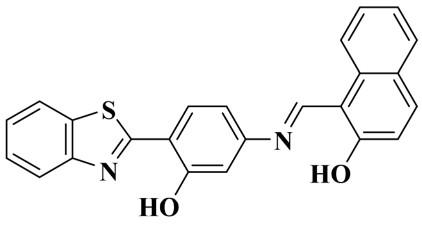

HNBZT-II

Three low-lying excitations of **HNBZT-I** and **HNBZT-II** were calculated in accordance with S_0 geometry in order to investigate the photoexcitation process. Table 2 contains a tabulation of the computed excitations. With an oscillation strength of 1.2213 at 419 nm for $S_0 \rightarrow S_1$ excitation, the TDDFT calculation for **HNBZT-I** showed an orbital transition contribution of 98.5% from the highest occupied molecular orbital (HOMO) to the lowest unoccupied molecular orbital (LUMO), which is close to the experimental absorption peak at 405 nm. In contrast, $S_0 \rightarrow S_1$ excitation for **HNBZT-II** was calculated at 416 nm, with an orbital contribution of 98.5% from the HOMO to LUMO transition and oscillation strength of 1.2079. We have only taken into consideration the $S_0 \rightarrow S_1$ excitation for further analysis because the calculated $S_0 \rightarrow S_2$ and $S_0 \rightarrow S_3$ excitations have low oscillation strengths for both configurations.

Furthermore, both qualitative and quantitative assessments were made for the change in electronic distribution. For both configurations, **HNBZT-I** and **HNBZT-II**, the involved molecular orbitals showed a shift in electron density from the benzothiazole unit (in the HOMO) to the Schiff base unit (in the LUMO) (Fig. 2). The ensuing hole–electron analysis revealed a large distance of electron/hole centroid (D = 7.953 Å for **HNBZT-I** and 7.863 Å for **HNBZT-II**) and a low overlap integral (S_r = 0.42174 for **HNBZT-I** and S_r = 0.42741 for **HNBZT-II**) of hole/electron distribution, establishing an intramolecular charge transfer process in **HNBZT** for both configurations.

Table 2 Summary of excitation spectra of **HNBZT-I** and **HNBZT-II**

HNBZT-I			**HNBZT-II**		
Excitation	λ (nm)	MO	Excitation	λ (nm)	MO
$S_0 \rightarrow S_1$	419.72 (f = 1.2213)	H → L (98.5%)	$S_0 \rightarrow S_1$	416.66 (f = 1.2079)	H → L (98.5%)
$S_0 \rightarrow S_2$	363.29 (f = 0.0216)	H-1 → L (95%)	$S_0 \rightarrow S_2$	360.66 (f = 0.0261)	H-1 → L (96%)
$S_0 \rightarrow S_3$	332.23 (f = 0.0757)	H-2 → L (89.6%)	$S_0 \rightarrow S_3$	333.26 (f = 0.0760)	H-2 → L (59%), H-4 → L (15%), H → L + 1 (14%)

λ = calculated excitation wavelength (nm); MO = molecular orbitals contributing to excitations; H = HOMO; L = LUMO.

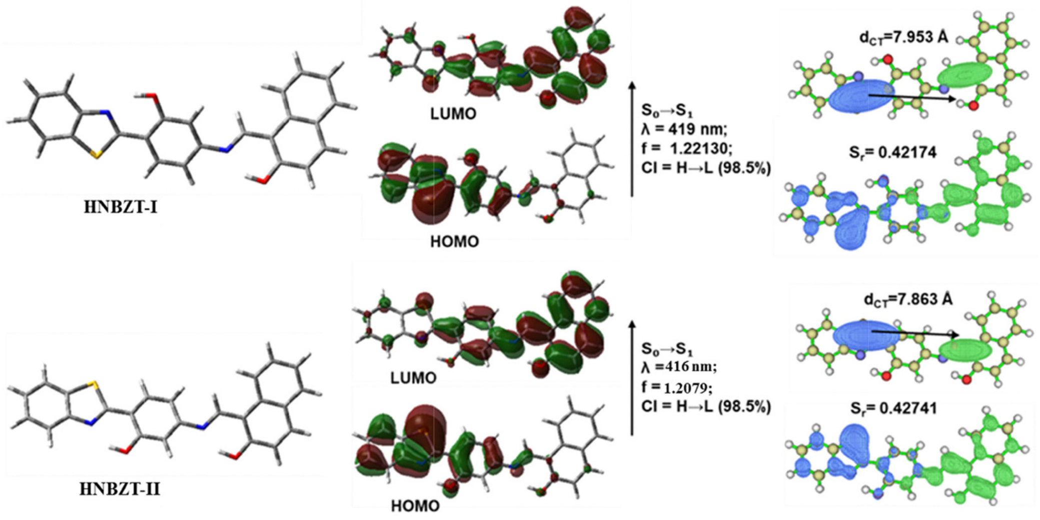

Fig. 2 Optimized structures of **HNBZT** along with their frontier molecular orbitals.

3.2. Geometrical parameters and tautomeric conversion

HNBZT contained two kinds of asymmetrical intramolecular hydrogen bonding (IraHB) labeled as A and B with short interaction distance (less than the sum of van der Waals radii of hydrogen and nitrogen) and angles. For **HNBZT-I**, on photoexcitation to S_1 state, the intramolecular distances for A type interaction were decreased from 1.686 Å to 1.635 Å, while the bond angle increased from 146.80° to 149.23°. On the other

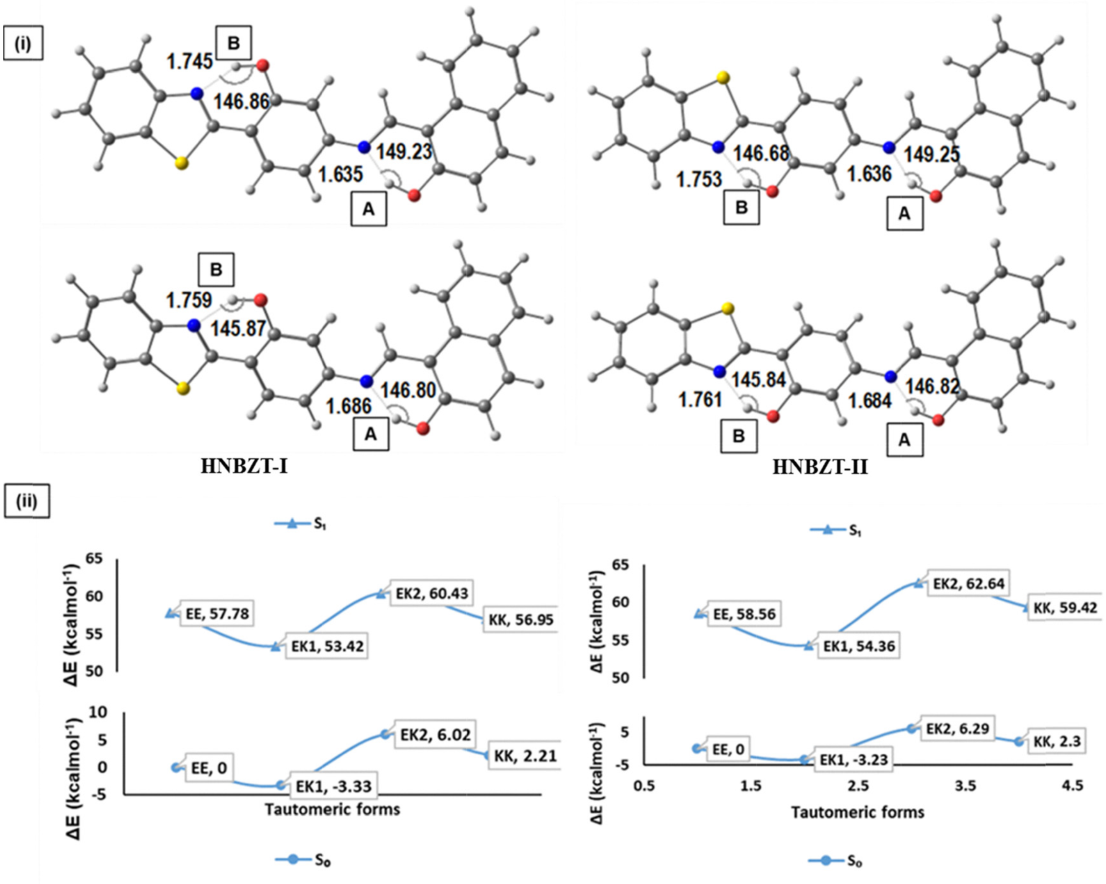

Fig. 3 (i) Optimized structures of **HNBZT-I** and **HNBZT-II** along with significant geometrical parameters and (ii) energy profile of the tautomeric forms at S_0 and S_1.

hand, B type interaction showed a decrease in distance from 1.759 Å to 1.745 Å, while the bond angle increased from 145.87° to 146.86°. A similar trend was observed for the **HNBZT-II** conformer too. It was also noted that a significant molecular planarity was achieved with a decrease of dihedral angle of the Schiff base unit for both conformers in the S_1 state. These alterations in bond distance and angle (on photoexcitation) established strengthening of intramolecular hydrogen bonding, which could prompt the proton transfer process in the excited state (Fig. 3). Therefore, the tautomeric conversion through the proton transfer process in **HNBZT** could result in four different tautomeric forms (EE, EK1, EK2, KK). The relative free energy (ΔG) profile of the tautomeric forms for **HNBZT-I** established a relationship of EE (0 kcal mol^{-1}) > EK1 (-3.33 kcal mol^{-1}) < EK2 (6.02 kcal mol^{-1}) > KK (2.21 kcal mol^{-1}) in the S_0 state and EE (57.78 kcal mol^{-1}) > EK1 (53.42 kcal mol^{-1}) < EK2 (60.43 kcal mol^{-1}) > KK (56.95 kcal mol^{-1}) in the S_1 state. A similar trend has been observed for **HNBZT-II**.

3.3. Aggregation induced emission (AIE) studies

Aggregation-induced emission (AIE) characteristics are commonly observed in organic fluorophores containing rotor structures. We investigated the AIE effect of the naphthalene rotor in **HNBZT** by conducting experiments in CH_3CN/H_2O mixtures with varying H_2O content. The absorption spectra of **HNBZT** exhibited a blue shift from 400 nm to 355 nm as the H_2O content increased from 0% to 50%. However, as the H_2O fraction increased from 60% to 100%, the absorption intensity progressively increased, accompanied by a noticeable red shift from 355 nm to 480 nm and the appearance of a levelling-off tail in the absorption band (Fig. 4a). The bathochromic shift observed is associated with the formation of J-type aggregates. Further variations in the emission spectra of **HNBZT** were observed with changing the H_2O percentages in the CH_3CN solutions (0–100%). As the H_2O fraction increased, the emission intensity also increased significantly (Fig. 4b). This enhancement in emission intensity is attributed to the aggregation-induced emission (AIE) process in **HNBZT**. The visible color change from dark yellow to pale of the **HNBZT** solution upon increasing the H_2O ratio was observed, which is attributed to Mie scattering and the aggregation of **HNBZT** with increasing H_2O content (Fig. 4c). Thus, the observed tailing between 450–550 nm in Fig. 4a is characteristic of aggregate formation, and this aggregate-induced emission enhancement is supported by emission spectra, DLS, and FESEM results. Regarding the emission spectra, intermolecular hydrogen bonding with water would typically shift the parent emission of **HNBZT** to a shorter

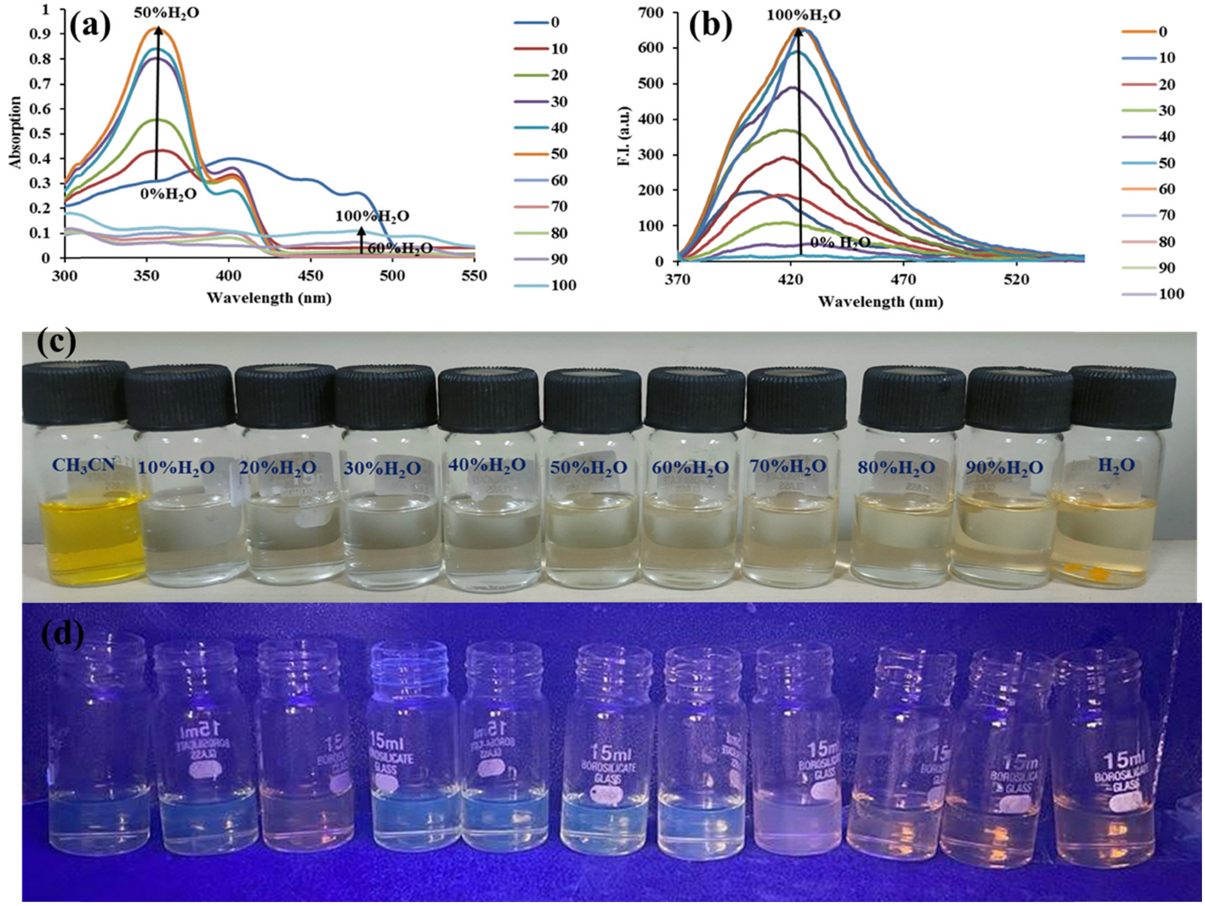

Fig. 4 (a) Absorption and (b) emission spectra of **HNBZT** with increasing H_2O ratio in CH_3CN. (c) Colorimetric and (d) emission response of **HNBZT** upon increasing H_2O content in CH_3CN.

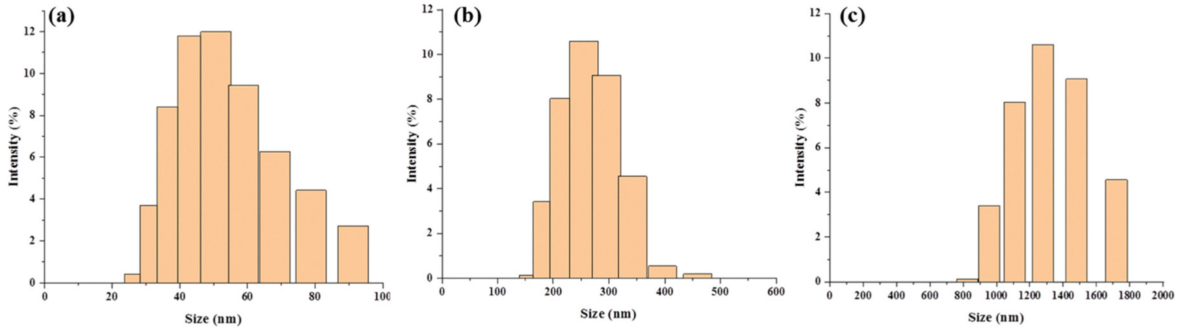

Fig. 5 DLS of **HNBZT** in (a) CH_3CN, (b) 50% $CH_3CN:H_2O$ and (c) H_2O.

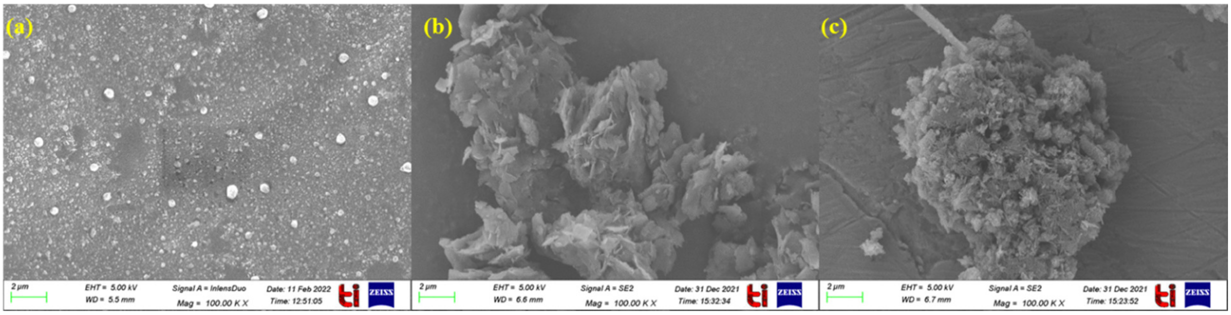

Fig. 6 FESEM images of **HNBZT** in (a) CH_3CN, (b) 50% $CH_3CN:H_2O$ and (c) H_2O.

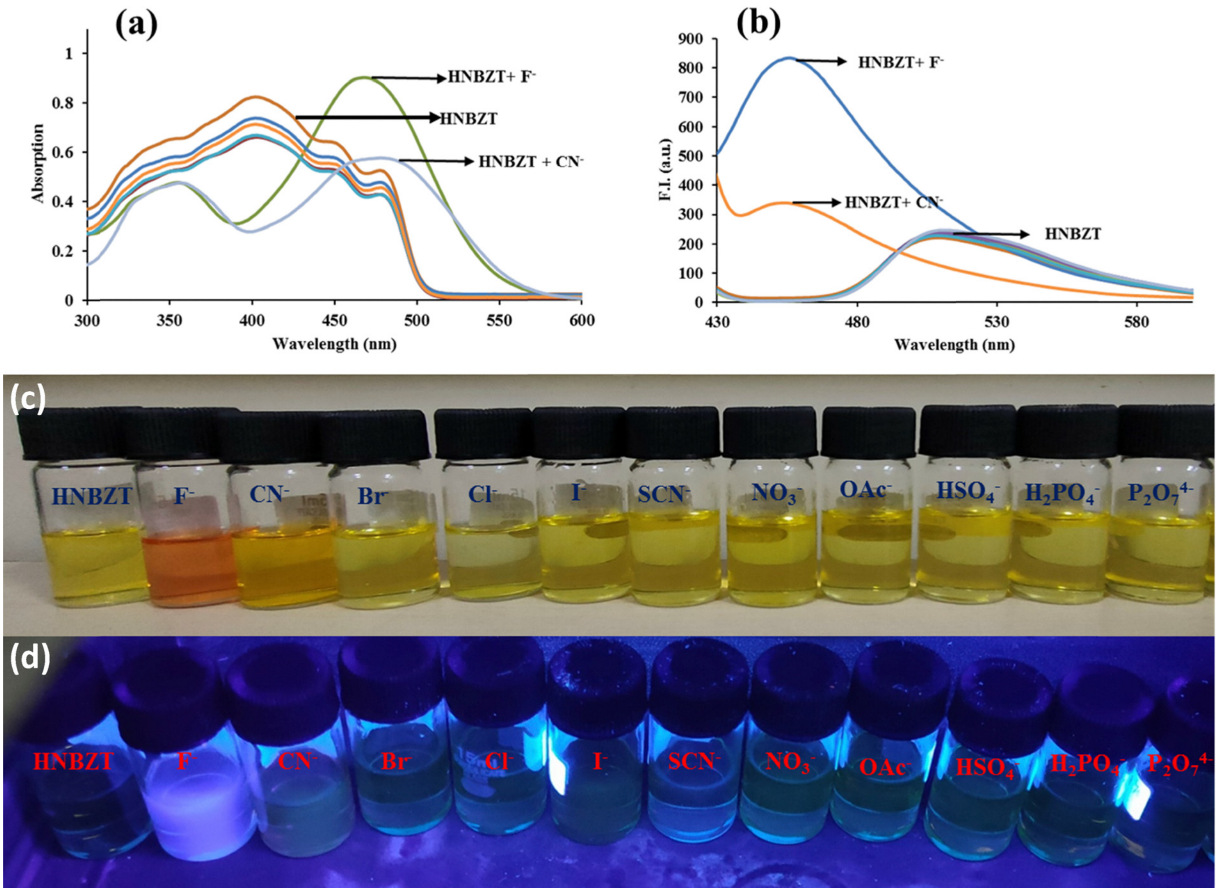

Fig. 7 (a) Absorption and (b) emission spectra of **HNBZT** (20 μM) upon interaction of different anions (1000 μM) in CH_3CN. (c) Colorimetric and (d) fluorogenic responses of **HNBZT** (20 μM) upon interaction with different anions in CH_3CN.

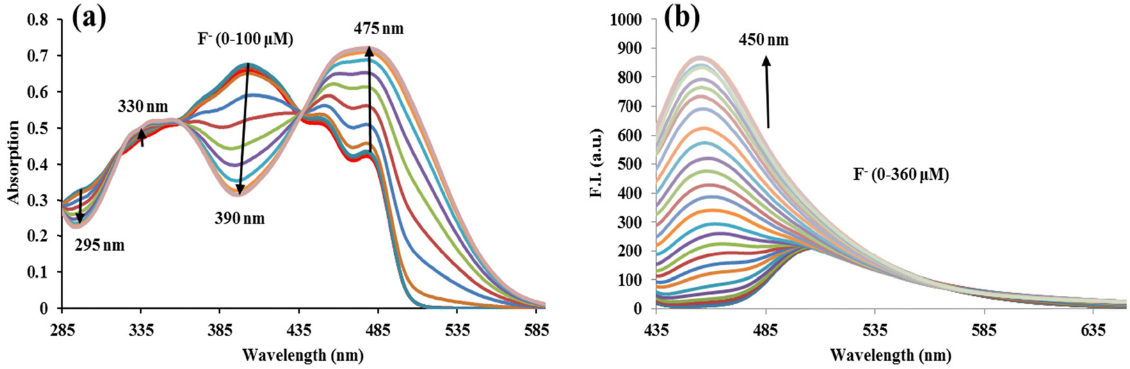

Fig. 8 (a) Absorption spectra of **HNBZT** upon incremental addition of 0–100 μM of F^- ions and (b) emission spectra of **HNBZT** upon incremental addition of 0–360 μM of F^- ions.

wavelength, as seen in its interactions with F^- and CN^- ions. The characteristic keto emission at 515 nm arises from intact intramolecular hydrogen bonding in **HNBZT**, whereas disruption of this bonding results in enol-type emission around 450 nm. This behaviour is further supported by theoretical calculations.

To investigate the aggregation behaviour of **HNBZT**, dynamic light scattering (DLS) experiments were conducted. The results confirmed the aggregation behaviour of **HNBZT** and provided insights into the size of aggregates under varying $CH_3CN:H_2O$ ratios. In pure CH_3CN, the aggregate size ranged from 20–100 nm, with an average size of 50 nm and a polydispersity index (PDI) of 0.3. In a 50% $CH_3CN–H_2O$ mixture, the aggregate size increased to 100–500 nm, with an average size of 250 nm and a PDI of 0.6. This hydrodynamic diameter further increased significantly to 1250 nm in pure H_2O, with a PDI value of 0.8 (Fig. 5). Field emission scanning electron microscopy (FESEM) analysis supported these findings, showing particle sizes of 20 nm in pure CH_3CN, 150 nm in 50% $CH_3CN–H_2O$, and 993 nm in pure H_2O (Fig. 6). The coherence between the DLS and FESEM results underscores the consistency and reliability of the observed aggregation behaviour of **HNBZT**.

3.4. Anion binding behavior of HNBZT

The binding behavior of **HNBZT** (20 μM) toward various anions was investigated in CH_3CN. As previously discussed, **HNBZT** exhibited a high-energy transition band at 400 nm and two low-energy transition bands at 445 nm and 475 nm in the absorption spectrum. A weak emission band was observed at 505 nm upon excitation at 400 nm. The anion-binding affinity of **HNBZT** was examined in the presence of different anions, including F^-, Cl^-, Br^-, I^-, $H_2PO_4^-$, NO_3^-, AcO^-, HSO_4^-, $P_2O_7^{4-}$, CN^-, and SCN^- using absorption and emission spectroscopy where **HNBZT** demonstrated a strong binding affinity for F^- and CN^- anions. For both F^- and CN^-, the absorption band at 475 nm intensified with a quantum yield of 0.81 and 0.79, respectively, while the bands at 400 nm and 445 nm disappeared (Fig. 7a). In the fluorescence spectra, the emission maximum of **HNBZT** at 505 nm underwent a blue shift to 450 nm upon interaction with F^- and CN^- anions (Fig. 7b). Additionally, **HNBZT** exhibited a notable colorimetric response, changing from light yellow to orange with F^- and to dark yellow with a CN^- anion (Fig. 7c) while **HNBZT** under UV light showed emission colour change from mild green fluorescence to purplish blue fluorescence in the presence of F^- ions (Fig. 7d). These results highlighted the strong binding and distinct optical responses of **HNBZT** to F^- and CN^- anions.

Table 3 Binding constants and detection limits of **HNBZT** for F^- and CN^- ions

	Binding constant	LOD
HNBZT + F^-	$2.9 \times 10^5\ M^{-1}$	7.6×10^{-8} M
HNBZT + CN^-	$7.5 \times 10^3\ M^{-1}$	1.1×10^{-7} M

Titration assays were presented to investigate the binding affinities of **HNBZT** for F^- and CN^- ions. In the absorption

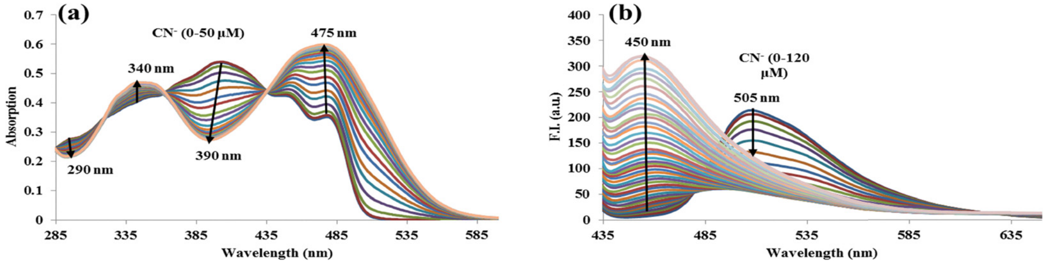

Fig. 9 (a) Absorption spectra of **HNBZT** upon incremental addition of 0–50 μM of CN^- ions and (b) emission spectra of **HNBZT** upon sequential addition of 0–120 μM of CN^- ions.

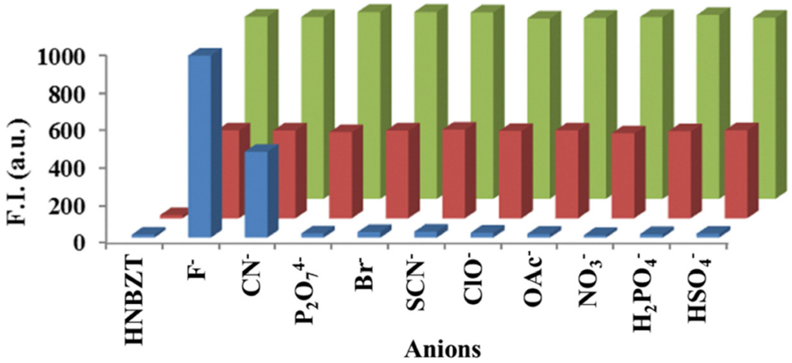

Fig. 10 Relative emission intensity of **HNBZT** (20 μM) in CH_3CN (λ_{ex} = 390 nm) with different competing anions in the absence and presence of F^- and CN^- ions at λ_{em} = 450 nm, where blue bars represent the emission intensity change of **HNBZT** with different anions (1000 μM), red bars represent **HNBZT** + CN^- in the presence of different relevant competing anions (1000 μM) and green bars represent **HNBZT** + F^-.

spectra, the band centered at 405 nm decreased with a slight blue shift to 390 nm, while the band at 475 nm intensified upon incremental addition of F^- (0–100 μM). Additionally, the absorption band at 330 nm showed a slight increase in intensity, whereas the band at 295 nm decreased. The formation of two isosbestic points at 435 nm and 355 nm indicated the equilibrium between multiple species (Fig. 8a). Similarly, emission titration experiments with sequential addition of F^- ions (0–360 μM) revealed an enhancement of the emission band at 450 nm, while the band at 515 nm disappeared (Fig. 8b). To determine the reaction stoichiometry between **HNBZT** and F^- ions, emission spectra were analyzed at different mole fractions of F^-. The emission maximum observed at a mole fraction of 0.5 indicated a 1 : 1 stoichiometry, determined with Job's plot analysis (Fig. S5a, ESI†).

Using the Benesi–Hildebrand equation, the binding constant for **HNBZT** and F^- was calculated to be $2.9 \times 10^5\ M^{-1}$. The lowest detection limit for F^- ions was determined to be 7.6×10^{-8} M, highlighting the high sensitivity of **HNBZT** for F^- detection.

Similar results were observed for the CN^- ion. During absorption titration, the band at 475 nm was increased, while the band at 405 nm decreased with a slight blue shift to 390 nm. Moreover, the absorption band at 340 nm revealed a slight increase in intensity, while the band at 290 nm decreased (Fig. 9a). The presence of two isosbestic points indicated an equilibrium between multiple species. In the emission titration, the emission band at 505 nm decreased, accompanied by an increase in emission intensity at 450 nm (Fig. 9b). The binding constant for CN^- was calculated to be $7.5 \times 10^3\ M^{-1}$, with the lowest detection limit of 1.1×10^{-7} M (Table 3). Job's plot analysis confirmed a 1 : 1 stoichiometry for the interaction between **HNBZT** and CN^- ions (Fig. S5b, ESI†).

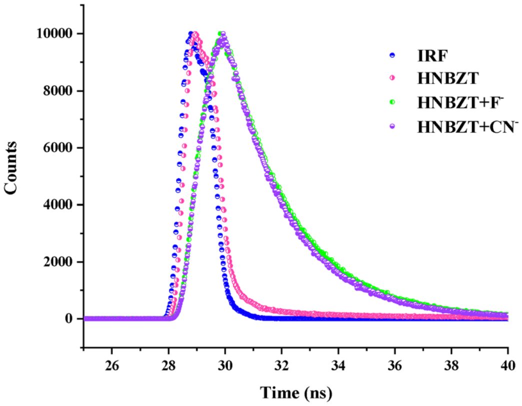

Fig. 11 Time resolved fluorescence decay of **HNBZT** and **HNBZT** with F^- and CN^- ions.

An interference study was also conducted to evaluate the selectivity of **HNBZT** toward F^- and CN^- ions. No significant changes were observed in the emission spectra of **HNBZT** + F^- and **HNBZT** + CN^- upon the addition of excess competitive anions (1000 μM), including F^-, CN^-, Br^-, SCN^-, ClO^-, AcO^-, NO_3^-, $P_2O_7^{4-}$, $H_2PO_4^-$, and HSO_4^- (Fig. 10). This demonstrated that **HNBZT** exhibits high selectivity for both F^- and CN^- anions.

3.5. Time-correlated single photon counting (TCSPC) study

The fluorescence enhancement behaviour of **HNBZT** upon binding with F^- and CN^- ions was further corroborated by time-correlated single photon counting (TCSPC) studies. The fluorescence decay profiles of **HNBZT** and its complexes were best fitted using a three-exponential function (Fig. 11). For **HNBZT**, three lifetime components were observed: 1.12 ns, 6.90 ns, and 0.07 ns, with population percentages of 7.32%, 8.45%, and 84.23%, respectively. The average lifetime of **HNBZT** was calculated to be 0.09 ns. Upon addition of F^- ions to **HNBZT**, the fluorescence decay revealed three components with lifetimes of 1.43 ns, 1.53 ns, and 2.44 ns, and corresponding population percentages of 27.85%, 39.02%, and

Table 4 Fluorescence lifetime measurements for **HNBZT** and its complexes with F^- and CN^- ions in CH_3CN

CH_3CN	τ_1 (ns)	τ_2 (ns)	τ_3 (ns)	α_1	α_2	α_3	χ^2	τ_{av} (ns)
HNBZT	1.12	6.90	0.07	7.32	8.45	84.23	1.12	0.09
HNBZT + F^-	1.43	1.53	2.44	27.85	39.02	33.14	1.18	1.71
HNBZT + CN^-	1.76	9.52	2.36	35.42	0.94	63.64	1.07	2.12

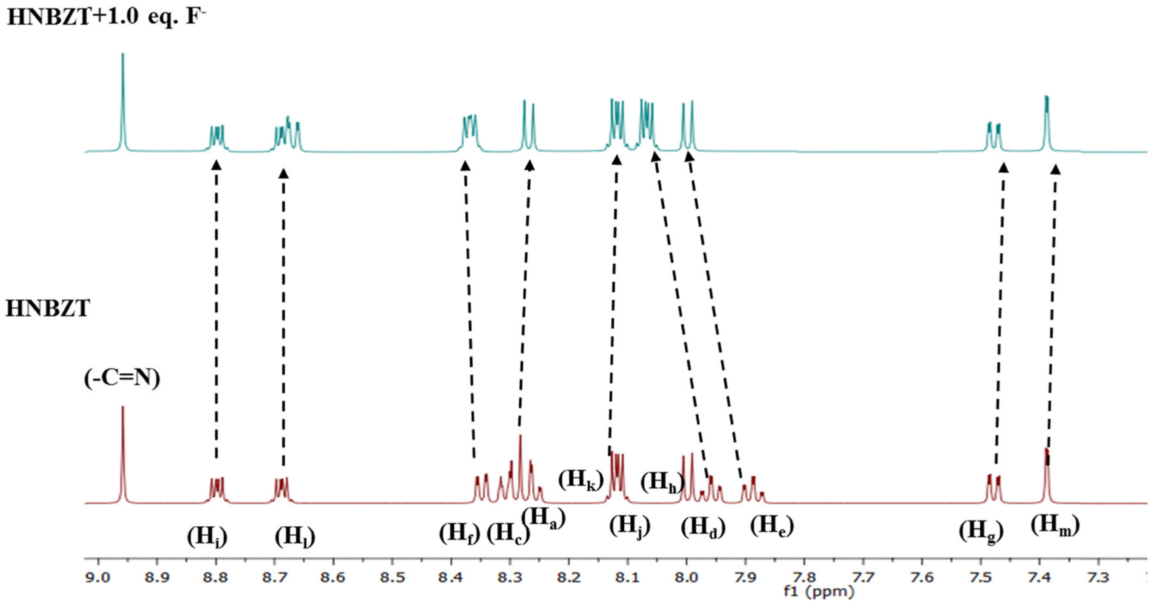

Fig. 12 ^{1}H NMR spectra of HNBZT with F^- ions in CD_3CN-d_3.

33.14%. The average lifetime was increased to 1.71 ns. Similarly, after the addition of CN^- ions to **HNBZT**, the average lifetime was increased from 0.09 ns to 2.12 ns (Table 4). The observed increase in average lifetime upon interaction with F^- and CN^- ions supports the fluorescence enhancement of **HNBZT** in the presence of these anions.

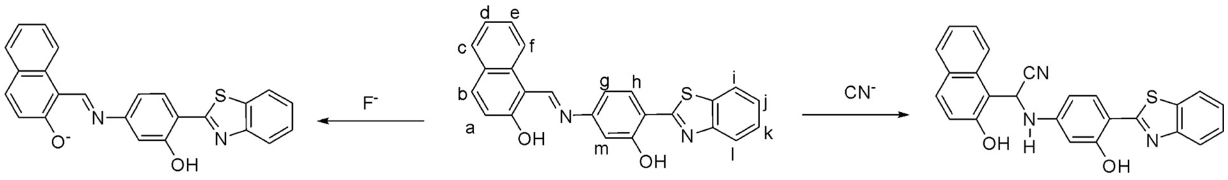

Scheme 2 Possible binding mechanisms of **HNBZT** with F^- and CN^- ions.

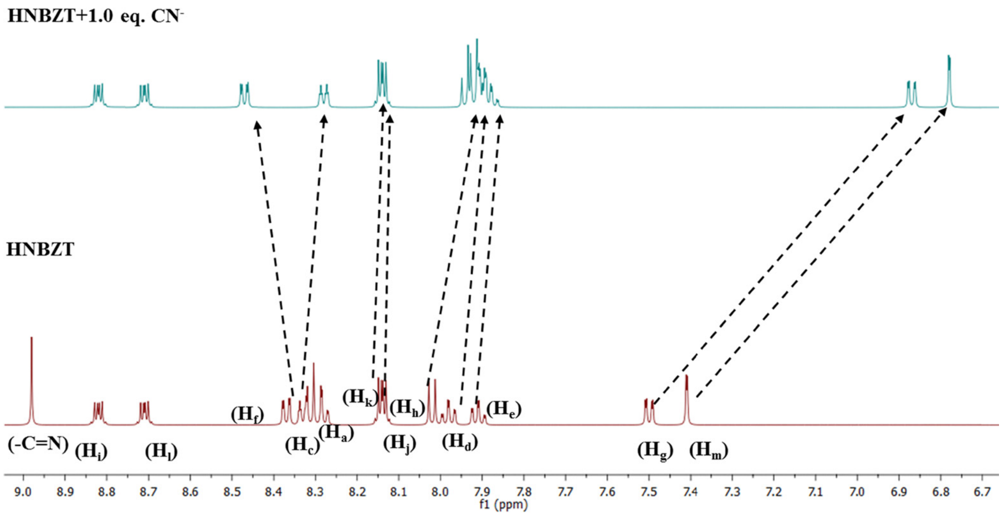

Fig. 13 ^{1}H NMR spectra of **HNBZT** with CN^- ions in CD_3CN-d_3.

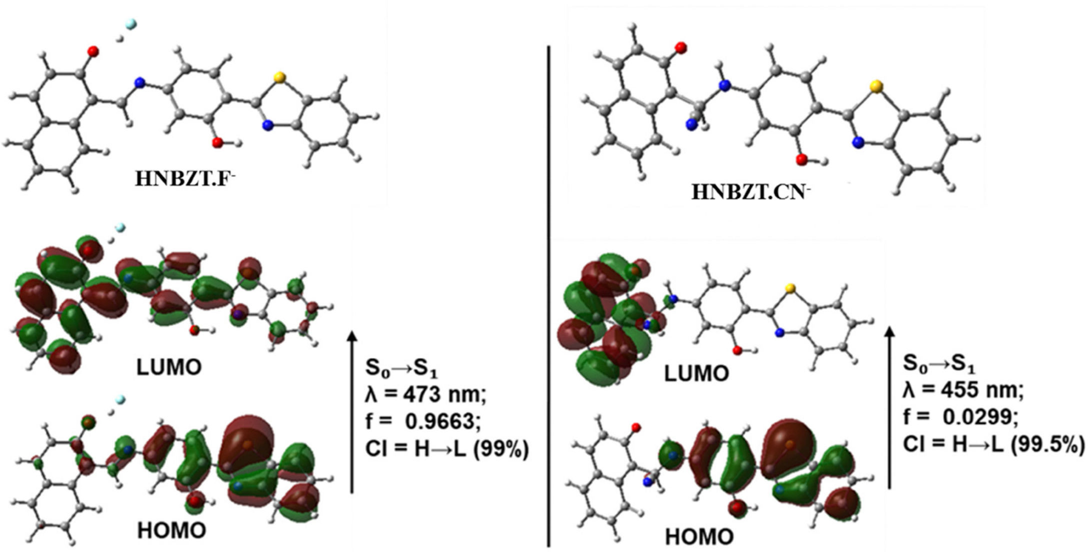

Fig. 14 Optimized structures of **HNBZT**.F^- and **HNBZT**.CN^- along with their frontier molecular orbitals.

3.6. ^{1}H NMR of HNBZT with F^- and CN^- ions

To investigate the binding mechanisms of F^- and CN^- ions with **HNBZT**, ^{1}H NMR titrations were conducted in CD_3CN-d_3. In the ^{1}H NMR spectrum of **HNBZT**, an imine proton was observed at δ 8.98 ppm. No significant change was detected at this position upon the addition of 1.0 equivalent of F^- ions (Fig. 12). Additionally, the disappearance of the hydroxyl proton indicated hydrogen bonding between the F^- ion and the naphtholic hydrogen. Further changes were observed in the aromatic region upon the addition of F^- ions. The peak corresponding to the H_a proton at δ 8.28 ppm was shifted, and the peak for the H_d proton at δ 7.95 ppm shifted to δ 8.05 ppm. Similarly, the peak at δ 7.88 ppm due to the H_e proton shifted to δ 7.95 ppm. These shifts suggested charge delocalization and redistribution within the **HNBZT** molecule after binding with F^- ions, likely as a result of deprotonation. In contrast, the protons in the phenyl ring, appearing at δ 7.49–7.36 ppm and benzothiazole ring at δ 8.82 ppm and δ 8.68 ppm, showed negligible changes, indicating that the phenyl and benzothiazole moieties were not significantly involved in the interaction (Fig. S6, ESI†). These findings provided insights into the binding mechanism of F^- ions with **HNBZT** (Scheme 2).

Similarly, the addition of 1.0 equivalent of CN^- ions to **HNBZT** caused significant changes in the proton signals. The imine proton at δ 8.98 ppm disappeared completely upon interaction with CN^- ions (Fig. 13). Additionally, the phenyl ring protons at δ 7.49 and 7.38 ppm were shifted upfield, and the naphthalene ring protons merged, indicating charge propagation across the molecule. In contrast, the protons in the benzothiazole ring, appearing at δ 8.82 and 8.71, showed negligible changes, thus not involved in the interaction. These observations suggested that the binding mechanism involved nucleophilic addition of CN^- ions to **HNBZT** (Scheme 2). ^{13}C NMR was also performed to confirm the binding behaviour of **HNBZT** with CN^- ions. With the addition of 1.0 equivalent CN^- ions, a new peak appeared at 50.40 ppm indicating the nucleophilic addition of CN^- to **HNBZT** (Fig. S7, ESI†). The FTIR spectrum of **HNBZT** before and after the addition of CN^- also confirmed the binding mechanism (Fig. S8, ESI†).

The binding interactions of F^- and CN^- ions with **HNBZT** were further corroborated through theoretical calculations. The optimized structures of the **HNBZT**·F^- and **HNBZT**·CN^- complexes are shown in Fig. 14. The predicted absorption spectra based on these optimized structures were in good agreement with the experimental results. For **HNBZT**·F^-, three low-lying vertical excitations were identified: the HOMO → LUMO transition (99%; f = 0.9663) at 473 nm, the HOMO−1 → LUMO transition (77%; f = 0.2191) at 396 nm, and the HOMO → LUMO+1 transition (82%; f = 0.0373) at 362 nm. Similarly, for **HNBZT**·CN^-, three low-lying vertical excitations were observed: the HOMO → LUMO transition (99.5%; f = 0.0299) at 455 nm, the HOMO → LUMO+1 transition (89%; f = 0.2896) at 368 nm, and the HOMO−1 → LUMO transition (82%; f = 1.0059) at 358 nm. In both complexes, the HOMO → LUMO transitions

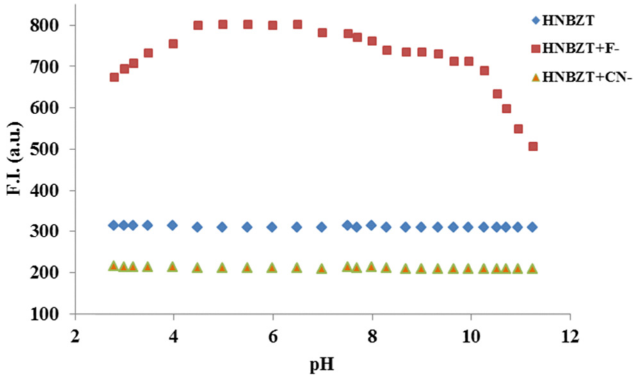

Fig. 15 Effect of pH on emission spectra of **HNBZT** (20 μM) and its complexes with ions in CH_3CN.

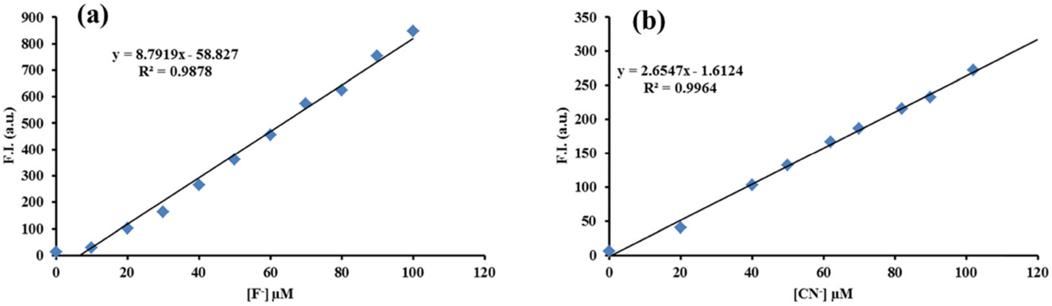

Fig. 16 Emission spectra of **HNBZT** in the presence of different concentrations of spiked (a) F⁻ and (b) CN⁻ from 0 to 100 μM.

exhibited a significant electron density shift from the benzothiazole unit to the Schiff base unit, indicating intramolecular charge transfer (ICT). This ICT is responsible for the observed colour changes in the presence of F⁻ and CN⁻ ions.

3.7. pH titration

We also checked the pH stability of **HNBZT** and its complex with the CN⁻ ions. To check the pH stability, we performed acid–base titration. From the acid–base titration, it is clear that our compound was stable in the pH range from 2–12 (Fig. 15). Similarly, the **HNBZT** and CN⁻ complex was also stable in the pH range of 2–12. The stability of **HNBZT** and its complex in the pH range 2–12 established its benefit for rapid monitoring in environmental and biological samples. The complex of **HNBZT** and F⁻ ions was also stable in the pH range from 4–10, so the detection of these ions using **HNBZT** could be well performed in a given pH range.

3.8. Detection of F⁻/CN⁻ ions in real samples

HNBZT was used to detect F⁻ and CN⁻ in real water samples in order to investigate the practical applicability of the chemosensor where satisfactory results were achieved. F⁻ and CN⁻ sample solutions were prepared using tap water from the laboratory. In this instance, known F⁻ and CN⁻ ion concentrations were directly spiked into tap water. The emission intensity was then measured at 450 nm after the samples were subjected to 20 μM of **HNBZT** in CH_3CN (Fig. 16). The favorable recoveries from tap water with varying F⁻ and CN⁻ ion concentration show practical applicability of **HNBZT** in everyday situations (Table 5). **HNBZT** can detect F⁻ and CN⁻ ions with high efficiency as compared to the previous reports (Table S1, ESI†). Similarly, good recoveries were obtained from toothpaste samples (Table 6).

Table 5 Determination of F⁻ and CN⁻ ions in tap water

Ion	Sample	Ion added (μM)	Ion recovered (μM)	Recovery (%)	RSD
F⁻	1	20	20.5	102.5	0.31
	2	40	41.1	102.75	0.35
CN⁻	1	20	18.1	90.5	0.42
	2	40	40.1	100.25	0.55

Table 6 Determination of F⁻ ions in toothpaste samples

Sample	F⁻ found	Added (μM)	Recovered (μM)	Recovery (%)	RSD
Toothpaste 1	1	10	9.5	95	0.71
	2	20	20.2	101	0.80
Toothpaste 2	1	10	9.9	99	0.78
	2	20	19.7	98.5	0.74

4. Conclusion

In conclusion, an efficient chemosensor, **HNBZT** was synthesized, and its photophysical properties were thoroughly investigated in various solvent systems. **HNBZT** demonstrated aggregation-induced emission (AIE) behaviour and was successfully employed for the selective and sensitive detection of F⁻ and CN⁻ ions in a CH_3CN solvent system. Detection of F⁻ and CN⁻ ions by **HNBZT** was achievable with the naked eye. The detection limits for F⁻ and CN⁻ ions were as low as 7.6×10^{-8} M and 1.1×10^{-7} M, respectively. ^{1}H NMR titration of **HNBZT** with F⁻ and CN⁻ ions revealed distinct binding mechanisms, with F⁻ ions forming hydrogen bonds, while CN⁻ ions induced nucleophilic addition which is also supported by theoretical studies. Notably, F⁻ and CN⁻ ions interacted with **HNBZT** *via* distinct binding mechanisms.

Conflicts of interest

There are no conflicts of interest to declare.

Data availability

The authors confirm that the data supporting the findings of this study are available within the article and/or its ESI.†

Acknowledgements

The authors would like to acknowledge CEEMS, TIET (TIET/CEEMS/Regular/2023/044) for financial support and DST-FIST (SR/FST/CS-II/2018/69) for HRMS analysis.

References

1 A. Mondal, P. Mondal and P. Chattopadhyay, Regulatory principles, parameters and probe design to ascertain the interconnection between ICT, ESIPT and PET mechanisms, *Inorg. Chim. Acta*, 2024, 122194.

2 R. M. Duke, E. B. Veale, F. M. Pfeffer, P. E. Kruger and T. Gunnlaugsson, Colorimetric and fluorescent anion sensors: an overview of recent developments in the use of 1,8-naphthalimide-based chemosensors, *Chem. Soc. Rev.*, 2010, **39**, 3936–3953.

3 P. Zhou and K. Han, ESIPT-based AIE luminogens: Design strategies, applications, and mechanisms, *Aggregate*, 2022, **3**, e160.

4 P. R. Dongare and A. H. Gore, Recent advances in colorimetric and fluorescent chemosensors for ionic species: Design, principle and optical signalling mechanism, *ChemistrySelect*, 2021, **6**, 5657–5669.

5 H.-W. Zheng, Y. Kang, M. Wu, Q.-F. Liang, J.-Q. Zheng, X.-J. Zheng and L.-P. Jin, ESIPT-AIE active Schiff base based on 2-(2′-hydroxyphenyl) benzo-thiazole applied as multi-functional fluorescent chemosensors, *Dalton Trans.*, 2021, **50**, 3916–3922.

6 M. Chen, Y. Chen, M. Zhong, D. Xie, C. Wang, X. Ren, S. Huang, J. Xu and M. Zhu, The Synergistic Mechanisms of AIE, ESIPT and ICT in the α-cyanostilbene-based Derivative: A Red-fluorescence Probe With a Large Stokes' Shift for Copper(II) Ion Determination and Reversible Response to Amine/acid Vapor, *J. Fluoresc.*, 2024, **34**, 1075–1090.

7 A. Mondal, E. Ahmmed, B. Ball and P. Chattopadhyay, Rational Design of a New AIE-Coupled ESIPT-Based Multichromic State Depended Organo-luminophore With Turn-on Emissive Response to Zn(II) in Aqueous and Solid-state, *ChemistrySelect*, 2022, **7**, e202103857.

8 J. Qin, B. Wang, Z. Yang and K. Yu, A ratiometric fluorescent chemosensor for Zn2+ in aqueous solution through an ESIPT coupled AIE process, *Sens. Actuators B*, 2016, **224**, 892–898.

9 J. Y. Shang, Y. Li, K. Chen and H. Li, Synthesis and properties of an AIE fluorescent probe for Cu2+ detection based on ESIPT system, *Chem. Pap.*, 2021, **75**, 1851–1859.

10 A. Jain, S. De, P. Saraswat, J. Haribabu, J. F. Santibanez and P. Barman, An ESIPT active coumarin-diphenyl azine-based AIEgen: Nanomolar Cu2+ ion sensing, Latent Fingerprinting, live-cell imaging, and real sample analysis, *J. Mol. Struct.*, 2024, **1310**, 138383.

11 S. Suresh, G. Prabakaran, J. Prabhu, P. Vijayanand, R. S. Kumar, R. Karthick, G. Velraj and R. Nandhakumar, A pyridine naphthalene conjugate: ESIPT based molecular chemosensor for Al3+ ions and sequential detection of H2PO4-and applications in milk, water samples and bio-imaging, *J. Food Compos. Anal.*, 2024, **132**, 106364.

12 U. Duraisamy, P. Jerome, N. Vijay and T. H. Oh, ESIPT: An approach and future perspective for the detection of biologically important analytes, *J. Lumin.*, 2023, 120350.

13 S. Paul, A. Ray Choudhury and N. Dey, Dual-mode multiple ion sensing via analyte-specific modulation of keto–enol tautomerization of an ESIPT active pyrene derivative: experimental findings and computational rationalization, *ACS Omega*, 2023, **8**, 6349–6360.

14 T. Jiang, J.-H. Lu, C. Huang, D.-M. Chen and B.-X. Zhu, Two helical Schiff bases with "AIE+ ESIPT" characteristics exhibiting selective ion recognition properties, *Dyes Pigm.*, 2024, **223**, 111972.

15 A. I. Said, N. I. Georgiev and V. B. Bojinov, Simple excited state intramolecular proton transfer (ESIPT) based probe for pH and selective detection of copper(II) ion in aqueous alkaline environment: Sensitivity, selectivity and logic behavior, *J. Photochem. Photobiol., A*, 2024, **446**, 115176.

16 F. Y. Wu, S. G. Cao and C. X. Xie, A highly selective chemosensor for copper ion based on ICT fluorescence, *Chin. Chem. Lett.*, 2012, **23**, 607–610.

17 C. I. David, P. Movuleeshwaran, H. Jayaraj, G. Prabakaran, M. S. Kumar, A. Abiram, T. S. Babu, J. Prabhu and R. Nandhakumar, Highly selective, reversible and ICT-based fluorescent chemosensor for bismuth ions: Applications in bacterial imaging, logic gate and food sample analysis, *J. Photochem. Photobiol., A*, 2022, **422**, 113558.

18 Pooja, H. Pandey, S. Aggarwal, M. Vats, V. Rawat and S. R. Pathak, Coumarin-based Chemosensors for Metal Ions Detection, *Asian J. Org. Chem.*, 2022, **11**, e202200455.

19 N. Kaur, Anthraquinone appended chemosensors for fluorescence monitoring of anions and/or metal ions, *Inorg. Chim. Acta*, 2022, **536**, 120917.

20 F.-Y. Ye, M. Hu and Y.-S. Zheng, Advances and challenges of metal ions sensors based on AIE effect, *Coord. Chem. Rev.*, 2023, **493**, 215328.

21 K. S. Jagadhane, S. R. Bhosale, D. B. Gunjal, O. S. Nille, G. B. Kolekar, S. S. Kolekar, T. D. Dongale and P. V. Anbhule, Tetraphenylethene-based fluorescent chemosensor with mechanochromic and aggregation-induced emission (AIE) properties for the selective and sensitive detection of Hg2+ and Ag+ Ions in aqueous media: application to environmental analysis, *ACS Omega*, 2022, **7**, 34888–34900.

22 M. H. Chua, B. Y. K. Hui, K. L. O. Chin, Q. Zhu, X. Liu and J. Xu, Recent advances in aggregation-induced emission (AIE)-based chemosensors for the detection of organic small molecules, *Mater. Chem. Front.*, 2023, **7**, 5561–5660.

23 M. D. Pandey, S. Asthana, M. V. Mouli, A. Tamrakar, M. A. Wani, A. K. Mishra and R. Pandey, Recent Advances in AIEgen-based Chemosensors for Small Molecule Detection, with a Focus on Ion Sensing, *Anal. Methods*, 2024, **16**, 4431–4484.

24 K. Krishnaveni, S. Gurusamy, K. Rajakumar, V. Sathish, P. Thanasekaran and A. Mathavan, Aggregation induced emission (AIE), selective fluoride ion sensing and lysozyme interaction properties of Julolidinesulphonyl derived Schiff base, *J. Photochem. Photobiol., A*, 2022, **427**, 113822.

25 L. Chen, H. Jiang, N. Li, Q. Meng, Z. Li, Q. Han and X. Liu, A Schiff-based AIE fluorescent probe for Zn2+ detection and its application as "fluorescence paper-based indicator", *Spectrochim. Acta, Part A*, 2022, **268**, 120704.

26 S. Zhang, D. Wu, X. Jiang, F. Xie, X. Jia, X. Song and Y. Yuan, A novel fluorescent probe with one-excitation and dual-emission for selective and simultaneous detection of Glutathione and Arginine in NIR and blue regions, *Sens. Actuators, B*, 2019, **290**, 691–697.

27 S. Ahamed, M. Mahato, R. Sahoo, N. Tohora, T. Sultana, A. Maiti and S. K. Das, Decoding the ICT-PET-ESIPT Liaison Mechanism in a Phthalimide-based Trivalent Transition Metal Ions Specific Chromo-fluorogenic Probe, *New J. Chem.*, 2024, **48**, 13131–13143.

28 A. Pramanik, R. Das, P. J. Boruah, S. Majumder and S. Mohanta, A very rare fluorescent chemosensor of zinc(II) exhibiting AIEE, ESIPT and TICT: Spectroscopic, crystallographic and theoretical exploration, *Spectrochim. Acta, Part A*, 2024, **308**, 123780.

29 X. Zhang, X. Weng, Z. Yang, P. Zhao, W. Chen, Z. Wu, X. Zhuang and A. Chalcone-based Fluorescence Probe, for H_2S Detecting Utilizing ESIPT Coupled ICT Mechanism, *J. Fluoresc.*, 2024, **34**, 821–828.

30 S. Enbanathan, S. Munusamy, D. Jothi, S. M. Kumar, P. Seenu, M. F. Noor and S. K. Iyer, An AIE dynamic a highly selective and expeditious benzothiazole-pyrazine based colorimetric chemosensor for Ni^{2+} and fluorogenic chemosensor for Cu^{2+} and Al^{3+} detection, *J. Mol. Liq.*, 2024, **404**, 124949.

31 B. Devi, A. K. Guha and A. Devi, Fluoride ion detection in aqueous medium: Colorimetric and turn-off fluorescent Schiff base chemosensor, *Spectrochim. Acta, Part A*, 2024, **305**, 123448.

32 H. M. Al-Saidi and S. Khan, Recent advances in thiourea based colorimetric and fluorescent chemosensors for detection of anions and neutral analytes: a review, *Crit. Rev. Anal. Chem.*, 2024, **54**, 93–109.

33 A. Palta, G. Kumar, K. Paul and V. Luxami, Highly selective colorimetric and fluorescent probe for F^- and $P_2O_7^{4-}$ based on AIEE and dual ESIPT, *J. Mol. Struct.*, 2024, 138880.

34 M. Ilakiyalakshmi, A. A. Napoleon, Phenothiazine-derived fluorescent chemosensor: a versatile platform enabling swift cyanide ion detection and its multifaceted utility in paper strips, environmental water, food samples and living cells, *J. Photochem. Photobiol., A*, 2024, **447**, 115213.

35 C. I. David and H.-i Lee, Cutting-edge advances in colorimetric and fluorescent chemosensors for detecting lethal cyanide ion: A comprehensive review, *Microchem. J.*, 2024, 110359.

36 W. Bouali, M. Yaman, N. Seferoğlu and Z. Seferoğlu, Colorimetric and fluorimetric detection of CN^- ion using a highly selective and sensitive chemosensor derived from coumarin-hydrazone, *J. Photochem. Photobiol., A*, 2024, **448**, 115227.

37 C. K. Maurya and P. K. Gupta, Discriminative Chromogenic Detection of Fluoride and Cyanide Ions, *ChemistrySelect*, 2024, **9**, e202304016.

38 B. S. Cugnasca, F. Duarte, J. L. P. de Albuquerque, H. M. Santos, J. L. Capelo-Martínez and C. Lodeiro, A. A. Dos Santos, Precision detection of cyanide, fluoride, and hydroxide ions using a new tetraseleno-BODIPY fluorescent sensor, *J. Photochem. Photobiol., A*, 2024, **457**, 115881.

39 A. Palta, S. Sharma, G. Kumar, D. Choudhary, K. Paul and V. Luxami, A highly specific benzothiazole-based Schiff base for the ratiometric detection of hypochlorite (ClO^-) ions in aqueous systems: a real application in biological imaging, *New J. Chem.*, 2024, **48**, 15402–15413.